Surfaces and Interfaces 72 (2025) 107393

Contents lists available at ScienceDirect

Surfaces and Interfaces

journal homepage: www.sciencedirect.com/journal/surfaces-and-interfaces

Surface condition, structure and phase composition of carbon steel irradiated with an intense pulsed ion beam

Natallia Poliak *, Victor Anishchik

Belarusian State University, Minsk 220030, Belarus

ARTICLE INFO

Keywords:
Intense pulsed ion beam
Surface modification
Craters
Texture
Elastoplastic characteristics
Friction coefficient

ABSTRACT

The effect of irradiation with an intense pulsed ion beam of hydrogen (30%) and carbon (70%) at accelerating voltage of 250 kV and an energy density of 0,6 and 1,6 J/cm^2 with a single pulse of 100 ns duration on the surface condition, structure, phase composition, elastoplastic and tribomechanical properties of carbon steel 65 was studied. Atomic force and scanning electron microscopy revealed smoothing of the surface relief and the formation of craters on it, while the average surface roughness decreases by 2-3 times compared to the initial one, and an increase in energy density leads to an increase in the average diameter of craters from 4 to 6 μm and their surface density from 2×10^8 to 8×10^8 m^{-2}. X-ray diffraction studies conducted in the grazing incidence diffraction geometry and Bragg-Brentano identified a change in the predominant orientation of crystallites in the near-surface layer, comparable in magnitude to the projective range of ions, and to a change in the phase composition in a wider layer, significantly exceeding it: the appearance of new phases and an increase in their volume fraction with increasing energy density. Instrumental indentation revealed changes in hardness and elastic-plastic characteristics of the near-surface layer of the samples. After IPIB exposure the friction coefficient decreased by 1.5 times. The observed changes are caused by rapid heating, melting, and solidification of the near-surface layer of the target and are caused by the processes of redistribution of elements, accumulation of defects, the course of structural and phase transformations, and the local stresses growth in the modified layer.

1. Introduction

Currently, for surface modification of metals and alloys, methods using concentrated energy flows of charged particles are often preferred [1–10]. The application of intense pulsed ion beams (IPIB) with power densities of 10^6-10^9 W/cm2 due to its high performance, lower energy consumption and environmental friendliness is a more effective method for modifying the near-surface layer of steels compared to traditional methods of their treatment – thermomechanical [11], thermochemical [12] and others. Such a range of power densities causes high-speed heating, up to melting, and ultrafast cooling of the near-surface layer of the target [2–4,6].

During IPIB irradiation, impurity atoms both included in the beam and in the atmosphere of the working chamber are implanted into the target; this is superimposed on the generation of shock waves, thermal fields, and thermomechanical stresses [4,5,13,14]. This leads to the creation of a modified layer at depths exceeding the projective ion run (long-range effect) [15]. The depth of the modified layer and the degree of change in properties depend on the IPIB parameters – energy density, duration and number of pulses. In the case of a mixed beam (carbon ions + hydrogen ions), the main energy release occurs closer to the target surface, which is due to the fact that the path of carbon ions is much smaller than that of hydrogen ions.

Under the action of IPIB, point defects and their complexes are formed in metals and alloys [5,16], the composition and structure of the near-surface layer change [4,5,17,18], phase transformations occur [16–19], surface morphology changes with relief smoothing [4,20,21] and crater formation [16,19,22–24], which leads to changes in their functional properties [1,2,4–6,14,21].

Earlier studies on the effect of IPIB on the structure and properties of α-Fe and steels of different classes and various applications have been carried out [4–6,18,19,21,25–28]. It should be noted that in some cases IPIB exposure can also lead to negative changes [27,28], which should be taken into account to achieve an optimal result.

Carbon steel 65 due to its low cost and good combination of mechanical properties (high strength, ductility, toughness and weldability), is used in mechanical engineering, petrochemical industry and nuclear power engineering for the manufacture of parts operated in quite harsh

* Corresponding author at: Faculty of Physics, Belarusian State University, Minsk 220030, Belarus.
E-mail addresses: poliak@bsu.by (N. Poliak), anishchik@bsu.by (V. Anishchik).

https://doi.org/10.1016/j.surfin.2025.107393
Received 7 March 2025; Received in revised form 9 July 2025; Accepted 8 August 2025
Available online 8 August 2025

conditions, so there is a need to reduce the roughness of their surface in order to effectively reduce the coefficient of friction [29]. Note that the surface of such parts should be not only hard enough to resist plastic deformation, but also elastic during load application. To ensure the best performance under external influences, it is necessary to select the optimal combination of elastic modulus and hardness. Instrumental indentation is an informative method for studying near-surface layers, which allows obtaining a wide range of elastic-plastic and mechanical characteristics [8,9,30]. It should be noted that there are not enough works devoted to studying the influence of IPIB on elastic-plastic and tribomechanical properties of steel 65 and similar steel compositions.

This work will allow us to obtain new experimental results on changes in surface morphology, texture coefficients, the structure of phase interfaces in a modified layer of steel 65, as well as elastoplastic characteristics (hardness, elastoplastic properties and friction coefficient). This will contribute to a deeper understanding of the effect of IPIB on the structure and functional characteristics of 65 steel products in order to ensure their durability in harsh operating conditions.

2. Materials and methods

2.1. Materials and samples

Pre-eutectoid carbon steel 65 with 0.65 wt. % C content was investigated in this work. The chemical composition of samples was as follows: 0.62–0.70% C, 0.50–0.80% Mn, 0,17–0,37% Si, Cr < 0,25 %, S < 0.035%, P < 0.035% by weight and Fe is base. The samples in the form of plates measuring (10×10×3) mm^3 after exposure at a temperature of 830 °C for 30 minutes were tempered in water, then mechanically polished from one side on sandpaper to a mirror shine. The standard heat treatment regime for steel 65 is quenching from 830 °C into oil and tempering at 470 °C. Quenching in water was chosen to increase the cooling rate in order to preserve the increased concentration of point defects [31].

Irradiation was carried on TEMP-4 accelerator by Tomsk Polytechnic University [6] by a beam of hydrogen (30%) and carbon (70%). In IPIB experiment, the peak value of accelerating voltage, pulse duration (FHWM) and number of irradiation, residual gas pressure in the chamber were 250 kV, 100 ns and 1 pulse, (2-5)×10^{-2} Pa, respectively. Pulse power density was ~1.5·10^7 W/cm^2, the ion current density – 25 and 65 A/cm^2, the energy density – 0.6 and 1.6 J/cm^2, respectively.

The simulations irradiation of carbon and hydrogen ions in carbon steel 65 were performed using SRIM-2013 in full-cascade mode [32]. In these simulations, displacement energies of 25 eV for iron, manganese, chrome and of 28 eV for carbon were employed, along with a material density of 7.85 g/cm^3. The concentrations of implanted ions and the displacement per atom (dpa) was converted considering the beam composition (H:C=3:7) into using equations (1) and (2) respectively:

$$C = \frac{N\left(\frac{atoms}{cm^3}\Big/\frac{atoms}{cm^2}\right) \times \varphi\ (ions/cm^2)}{\rho\ (atoms/cm^3)} \times\ 100\%, \tag{1}$$

$$dpa = \frac{\frac{vac}{ion\ (\text{Å})} \times 10^8}{\rho\ (atoms/cm^3)} \times \varphi\ (ions\,/\,cm^2), \tag{2}$$

where φ - the ion fluence, ρ - the atomic density of carbon steel (8.689×10^{22} atoms/cm^3) and vac/ion is the vacancy per ion ratio from SRIM. For ion current density J =25 A/cm^2 the fluence of hydrogen and carbon ions amounted to 0.5×10^{13} and 1.1×10^{13} cm^{-2}, for J = 65 A/cm^2 – 1.2×10^{13} and 2.9×10^{13} cm^{-2}, respectively.

2.2. Sample testing

The surface topography of the samples and profiles of craters was studied using an atomic force microscope (AFM) Solver P47 Pro (NT-MDT). The surface roughness values of the Sa and Sq samples were averaged over 5 different sites with the same sample area. The surface morphology was studied using a scanning electron microscope (SEM) LEO-1455 VP (Carl Zeiss) with secondary and backscattered electron detectors. The images were obtained at an accelerating voltage of 20 kV. The SEM images were obtained using the secondary electron mode (SE), which allows observing the surface relief, and the backscattered electron mode (BSD), when a phase contrast can be seen on the image of the sample surface. The elemental composition of the samples was determined by energy dispersive X-ray (EDX) microanalysis using an Aztec Energy Advanced X-Max 80 (Oxford Instruments) spectrometer. The Versa 3D DualBeam SEM (FEI Company) with an electron backscatter diffraction (EBSD) attachment was used to study the cross sections of the samples.

X-ray diffraction (XRD) studies of the samples were carried out on an Ultima IV (Rigaku) diffractometer. X-ray patterns were taken in CuKα radiation (wavelength λ = 0.15418 nm) in 0.05 degree increments in the grazing incidence X-ray diffraction (GIXRD) at 1 degree of incidence and Bragg-Brentano geometry within 2θ angle range 30–120 degree at room temperature. XRD analysis was carried out with the use of the database of the Joint Committee on Powder Diffraction Standard (JCPDS). The parameters of the α-Fe(a) and α'-Fe (a, c) crystal lattice were determined from the angular positions of the diffraction lines (211) and (112) - (211), respectively. The accuracy of determining the lattice parameters $\Delta a/a$ was ±0.0017.

The size of the regions of coherent scattering of X-rays L and magnitude of microstrain $\frac{\Delta d}{d}$ were calculated using formulas (3) [18] and (4) respectively:

$$L = \frac{0,9\lambda}{\beta_1 \times \cos\theta_1}\,(nm), \tag{3}$$

$$\frac{\Delta d}{d} = \frac{\beta_2}{4 \times tg\theta_2}, \tag{4}$$

where β_1 and β_2 - the full width at half maximum (FWHM) of the X-ray diffraction peaks (110) and (211) respectively, θ_1 and θ_2 - of the corresponding the Bragg angles.

The texture coefficient $TC_{(hkl)}$ of each reflex, which characterize the orientation of the crystallites and allow us to estimate how much they are oriented in a certain direction compared to a random orientation, were determined by the method described in [33,34], using the expression:

$$TC_{(hkl)} = \frac{\frac{I_{(hkl)}}{I_{0\,(hkl)}}}{\frac{1}{n}\sum_{i=1}^{n}\frac{I_{(hkl)}}{I_{0\,(hkl)}}}, \tag{5}$$

where $I_{(hkl)}$ - the reflex intensity (hkl) of the studied samples, n is the number of reflexes. The intensity values from JCPDS-00-006-0696 were used as the intensity values of the sample without texture $I_{0\,(hkl)}$.

The mechanical characteristics of the specimens were determined by instrumental indentation. Instrumental indentation measurements were performed according to ISO 14577-1 [30] on a DUH-202 instrument (Shimadzu) at room temperature. The load on the Berkovich diamond indenter was 0.294 N and the loading rate was 0.070 N/s, the dwell time under load was 10 s and the number of measurements was 10. Tribological tests were carried out on the tribometer UIPT-1 according to the scheme "finger-plane" at reciprocating motion of the specimen under conditions of dry friction at room temperature and air humidity of 40-50%. The load on the indenter made of tungsten carbide alloy was 0.49 N, its average speed was 2×10^{-3} m/s, the stroke length was 5×10^{-3} m, and the friction path was 5 m.

3. Results and discussion

3.1. Study of surface morphology and topography

Figures 1-5 show the results of studying the surface of the samples before and after exposure to ion beam. AFM and SEM images of its typical sections are shown in Figs. 1, 3. It can be seen that the processing significantly affects the condition of the surface of the samples: a decrease in its roughness is observed (Fig. 2) and the appearance of volumetric defects – craters (Fig. 3b, c).

The surface of the original sample (Fig. 3a) has microscratches that occurred during its preliminary mechanical preparation. After irradiation with an energy density of 0.6 J/cm^2, their traces become smaller (Fig. 3b), with an increase in energy density to 1.6 J/cm^2, they practically disappear (Fig. 3c), i.e. microscratches can be a kind of indicator of changes in the state of the surface layer when exposed to IPIB and indicate erosion and/or melting. As a result of irradiation, the average surface roughness *Ra* and the standard deviation *Rq* decrease by 2-3 times compared to the initial value (Figs. 1, 2), which correlates well with the SEM data (Fig. 3).

Craters are randomly distributed on the surface, they have different sizes, shapes and depths, while their profile predominantly is symmetrical in the depth of the target (Figs. 3b, c, 4 and 5). After treatment with Q = 1.6 J/cm^2, microcracks appear in the craters (Fig. 5c, d). With increasing energy density, the size distribution of craters and their number per unit area change markedly: the average diameter and surface density increase from 4 to 6 μm (Fig. 4a, b) and from 2×10^8 to 8×10^8 m^{-2} (Fig. 4c), respectively. EDX analysis of these regions showed an increased manganese content (Fig. 5c-d), their chemical composition is close to MC carbides. Considering that manganese is a more active carbide-forming element than iron, it can be assumed that complex carbides (FeMn)C are formed. The formation of microcracks in craters indicates increasing stresses in the near-surface layer. Hydrogen atoms, located mainly along grain boundaries, can also contribute to this process.

3.2. Study of the structure and phase composition

Fig. 6 shows the distributions of carbon, hydrogen ions and of dpa in the target from SRIM simulations. The dpa curves have two peaks, which are localized at 250 and 1050 nm and are caused by carbon and hydrogen ions. It can be seen that the amount of dpa produced by carbon ions significantly exceeds the amount of dpa caused by hydrogen ions, which is due to the difference in ion masses. The hydrogen concentration in the surface layer of the target also increases.

The results of the XRD analysis are shown in Figs. 7-9 diffractograms were taken in the geometries of a GIXRD (Figs. 7a-c) and Bregg-Brentano (Fig. 7d-f), which made it possible to analyze the structure and phase composition at different depths. In our case, the thickness of the layer studied using a GIXRD is about 1 μm, which is comparable to the average projected path Rp of carbon and hydrogen ions, equal to 0.27 and 1.1 μm (Fig. 6), respectively. When using by Bregg-Brentano geometry, a wider layer is analyzed. On X-ray patterns taken in the GIXRD geometry, in contrast to the Bregg-Brentano survey, a redistribution of the integral intensity of the diffraction lines is observed (Fig. 7a-c), which indicates a change in the predominant orientation of the crystallites (texture) in the modified layer. The results of the evaluation of the effect of IPIB processing on the change in texture coefficients $TC_{(hkl)}$ shown in Fig. 8.

It can be seen that with an increase in the energy density in the pulse from 0.6 to 1.6 J/cm^2, the intensity of texture maxima is redistributed, which means that in the near-surface layer, comparable in magnitude to the projective range of ions, the predominant orientation of crystallites changes. A change in the texture of the surface layer of steel, nickel, copper, and aluminum under the influence of IPIB with modes similar to ours was observed earlier in [21,35].

Qualitative phase analysis showed (Fig. 7a-c) that reflections of ferrite and martensite are present on the XRD patterns of the initial sample. Martensite corresponds to double lines - "tetragonal doublets" (they determine the *c/a* ratio and carbon concentration) and they are located near to the lines (110), (200), (211) and (220) ferrite. The separation of the reflections of (211) ferrite and the "tetragonal doublet" (112)-(211) martensite in the range of angles 2θ = 78.8-84.2 degree is shown in Fig. 9, the parameters of the crystal lattice of the identified phases are shown in Table 1. As can be seen from Table 1, the ferrite lattice parameter practically does not change as a result of irradiation, the insignificant increases in the size of the coherent scattering regions *L* and the decrease in the magnitude of microstrain $\frac{\Delta d}{d}$. The reflex (211) of martensite (Fig. 9), by which the lattice parameter *a* is determined, shifts slightly, while reflex (112) (lattice parameter *c*) first noticeably shifts towards large angles, and then assumes its initial position, therefore, the carbon concentration in martensite first decreases and then increases (Table 1).

After exposure to IPIB in the range of angles 2θ = 42.8-46.2 degree, a change in the intensity of the overall profile of the line is observed, which is associated with the formation of carbides (Fe_2C (JCPDS-00-036-1249), Fe_7C_3 (JCPDS-00-017-0333), Fe_5C_2 (JCPDS-00-051-0997), Fe_3C (JCPDS-00-034-0001)) and γ-Fe (JCPDS-01-071-4649). The reflexes of the phases synthesized during treatment with Q = 0.6 J/cm^2 have a very low intensity (Fig. 10), which indicates their low volume fraction. After treatment with Q = 1.6 J/cm^2, their intensity becomes noticeably higher, and their volume fraction increases accordingly. It should be noted that the small volume fractions of the formed phases and the presence of the most intense reflexes (110) ferrite and (101) - (110) martensite in the specified angular range does not allow us to unambiguously separate the reflexes of carbides, ferrite and martensite (Fig. 10).

3.3. Study of elastoplastic and tribomechanical properties

Fig. 11 shows typical "load-displacement" curves for samples before and after IPIB and results of friction coefficient measurement. The analysis shows that for the irradiated specimens the indenter penetration depth h_{max} after holding under the maximum load, the depth of the residual print h_0 after load removal and the elastic stiffness of the

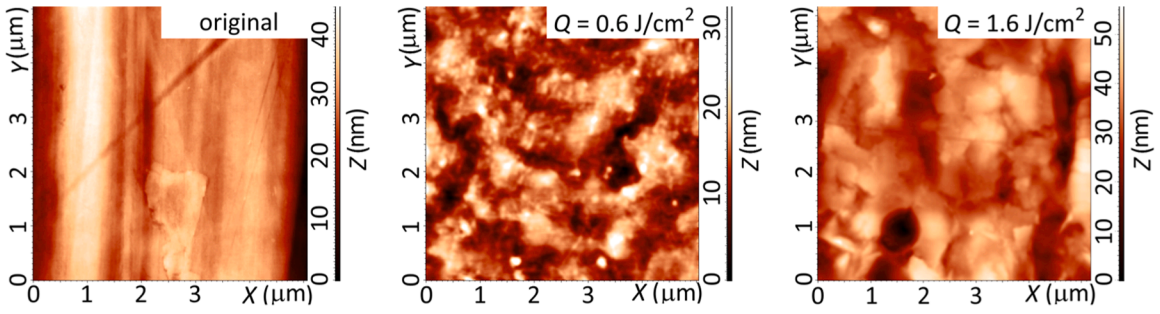

Fig. 1. AFM images of surface of the samples before and after exposure to an IPIB.

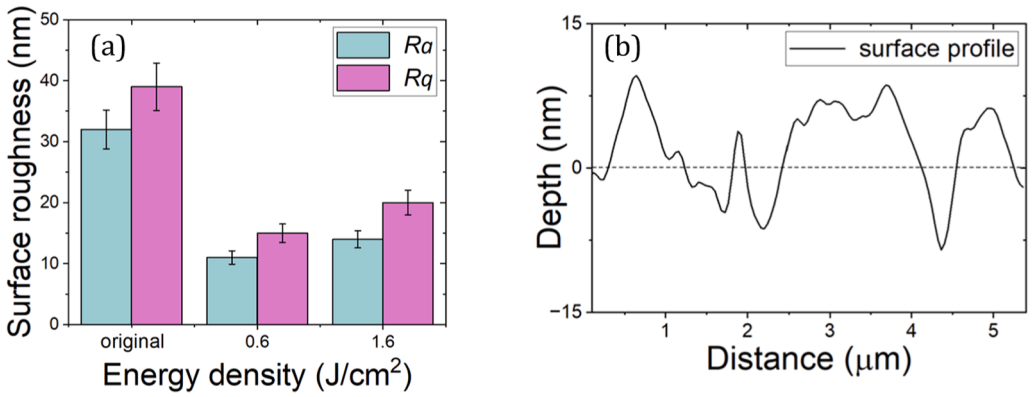

Fig. 2. Surface roughness parameters of the samples (a) and its typical profile (Q=0,6 J/cm^2) (b).

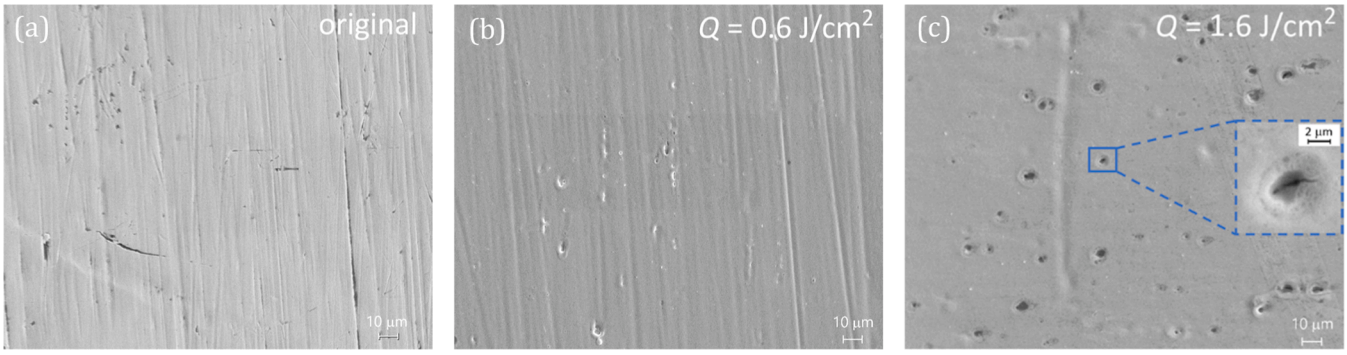

Fig. 3. Typical SEM-SE micrograph of surface of the samples before (a) and after exposure to an ion beam with Q=0,6 J/cm^2 (b) и Q=1,6 J/cm^2 (c).

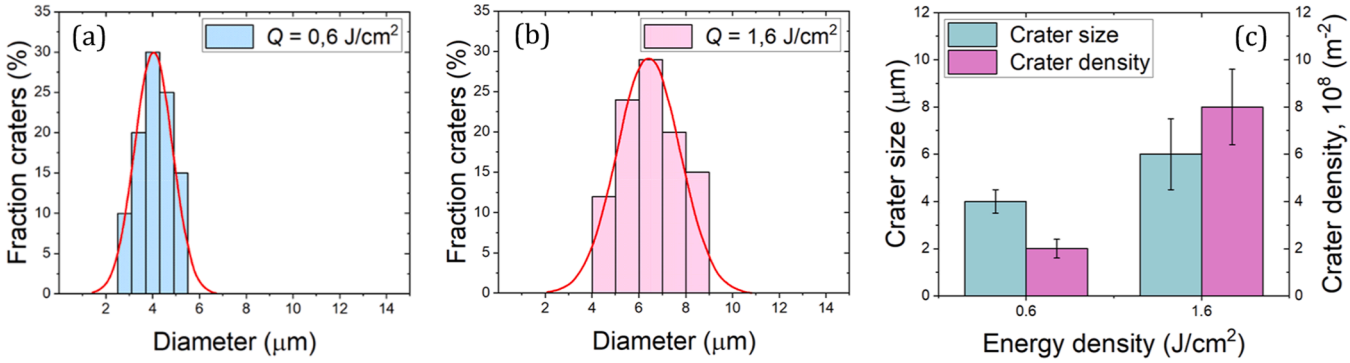

Fig. 4. Size distribution of craters for Q = 0,6 J/cm^2 (a) and Q = 1,6 J/cm^2 (b), histogram of changes in their size and density on the surface of samples (c).

material in the indenter print (slope of the initial section of the unloading branch) $S = dF/dh$ differ significantly from the corresponding data of the original specimen. The action of IPIB leads to the improvement of friction characteristics. As can be seen from Fig. 11b, e, h, for all samples, the coefficient of friction μ initially increases and then remains approximately constant. Thus, for the unirradiated specimen, initially there is a sharp increase of μ up to 0.70 (0.3 m), then its value is about 0.62. For the treated specimens, an increase in μ is observed at the initial stage to 0.47 and 0,50 for a friction path of 1.5 m and 1.0 m, then its values are 0.42 and 0.45, respectively for Q = 0.6 and 1.6 J/cm^2.

3.4. Discussion

It is known [1–5] that concentrated energy flows create conditions leading to melting and crystallization of the molten layer, while it is possible to change the surface relief. In [20], two mechanisms of surface smoothing were proposed: solid–phase and hydrodynamic. The mechanism of solid-phase smoothing during irradiation of a target with a rough surface is caused by the appearance of additional stress and strain fields in the surface layer of the target, contributing to a decrease in roughness, and operates up to the moment of melting. The hydrodynamic smoothing mechanism is activated after melting. As a result of the interaction of surface interaction forces, inertia forces caused by the accelerated movement of the surface layer of the target, and viscous forces, the amplitude of surface roughness decreases (Figs. 1-3). The removal of grinding marks during processing with an energy density of 1.6 J/cm^2 indicates that when exposed to IPIB, the target surface melts and its subsequent solidification occurs.

The formation of craters (Figs. 3-5) is a fairly common phenomenon in the surface treatment of metals and alloys of IPIB and may be associated with melting of the layer with evaporation of the target material [4]. In addition, the inhomogeneity of the ion density in the beam can

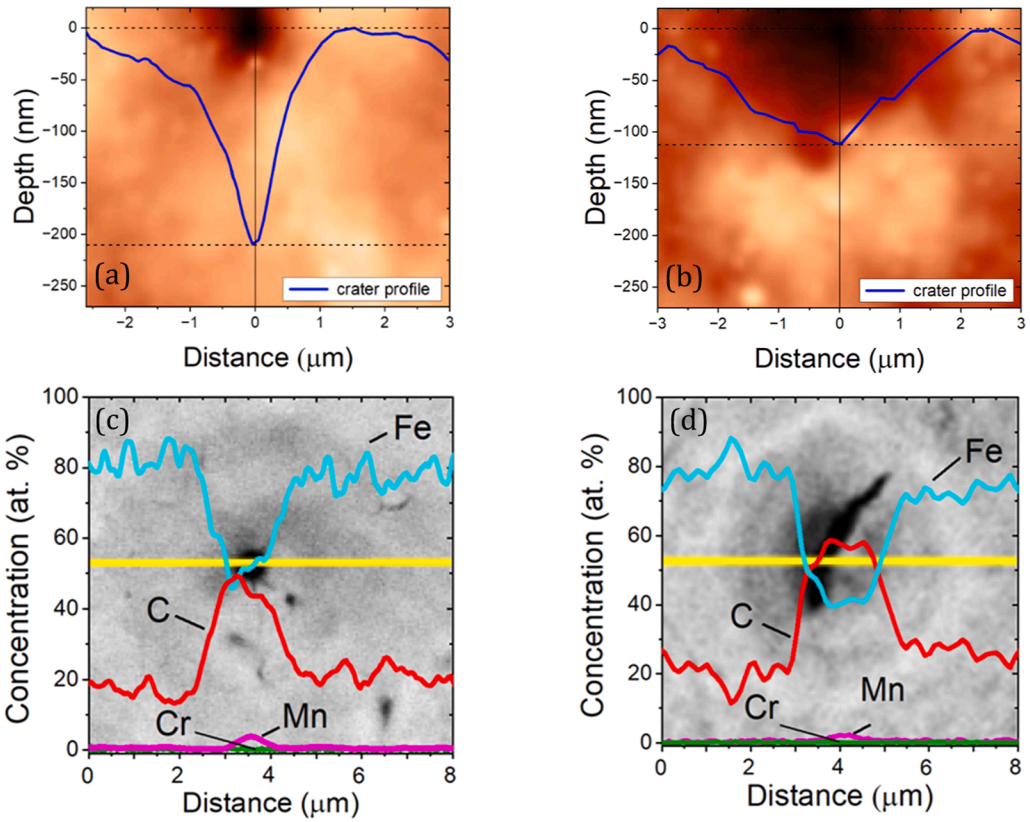

Fig. 5. Typical AFM (a, b) and SEM-BSD images (c, d) of craters illustrating their deep profiles (a, b) and EDX distributions (yellow line) (c, d) for samples treated with IPIB: $Q = 0{,}6$ J/cm^2 (a, b) and $Q = 1{,}6$ J/cm^2 (c, d).

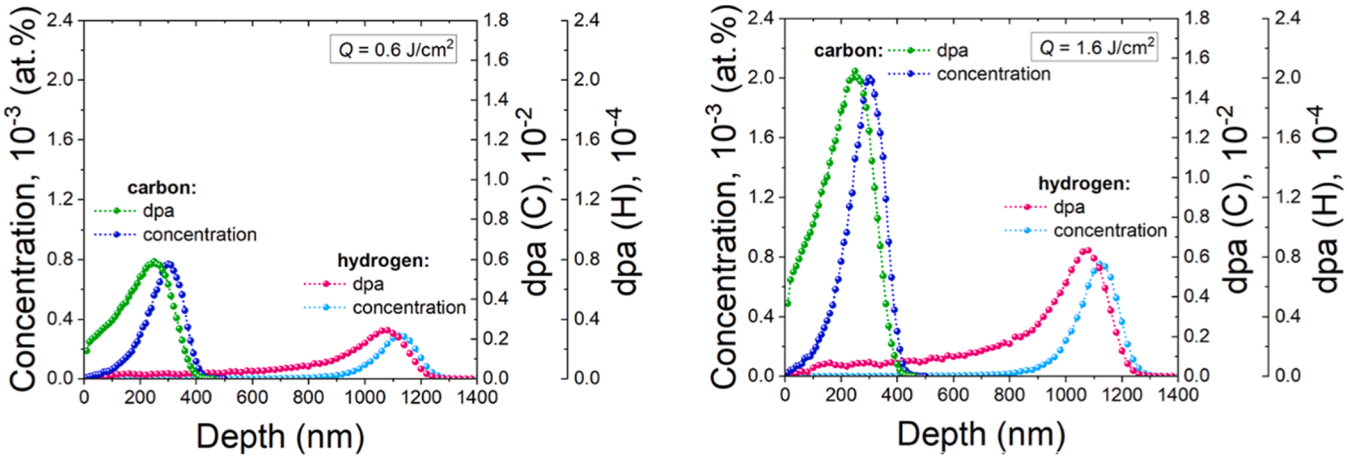

Fig. 6. SRIM simulations distribution of implanted hydrogen and carbon ions and distribution of displacement per atom (dpa) in the carbon steel 65.

also lead to the formation of areas of local melting and stress, which strongly affects crater formation. The presence of foreign inclusions and gas bubbles in the target volume is also an important factor in the formation of craters [36]. It should be noted that the presence of hydrogen in the ion beam increases the concentration of gas bubbles, which will be displaced to the surface during crystallization. It is noted in [19] that when IPIB is exposed to the surface of AISI 321 steel with an irradiation regime similar to ours, craters are formed, and sulfide or titanium-carbosulfide inclusions are preferred places for this. In our case, the EDX showed an increased content of carbon and manganese atoms in the craters (Fig. 5), as well as the presence of traces of sulfur in inclusions with manganese and chromium for the samples. The stresses formed in the target are maximal under the crater, which explains the observed localization of structural changes [24] and the appearance of microcracks.

The redistribution of the integral intensity of the diffraction lines with an increase in the density of the ion current in the pulse indicates that in the near-surface layer, comparable in magnitude to the projective range of ions, the predominant orientation of the crystallites changes (Fig. 7), and may be due to the dependence of the rate of crystallization and recrystallization processes on the crystallographic direction in the target grains, the local distribution of temperature fields of complex configuration and the associated thermomechanical stresses.

The change in the phase composition of the near–surface layer (Figs. 7, 9, 10) under pulsed ion irradiation with a power density greater than 10^7 W/cm^2 is associated with a number of processes: heating,

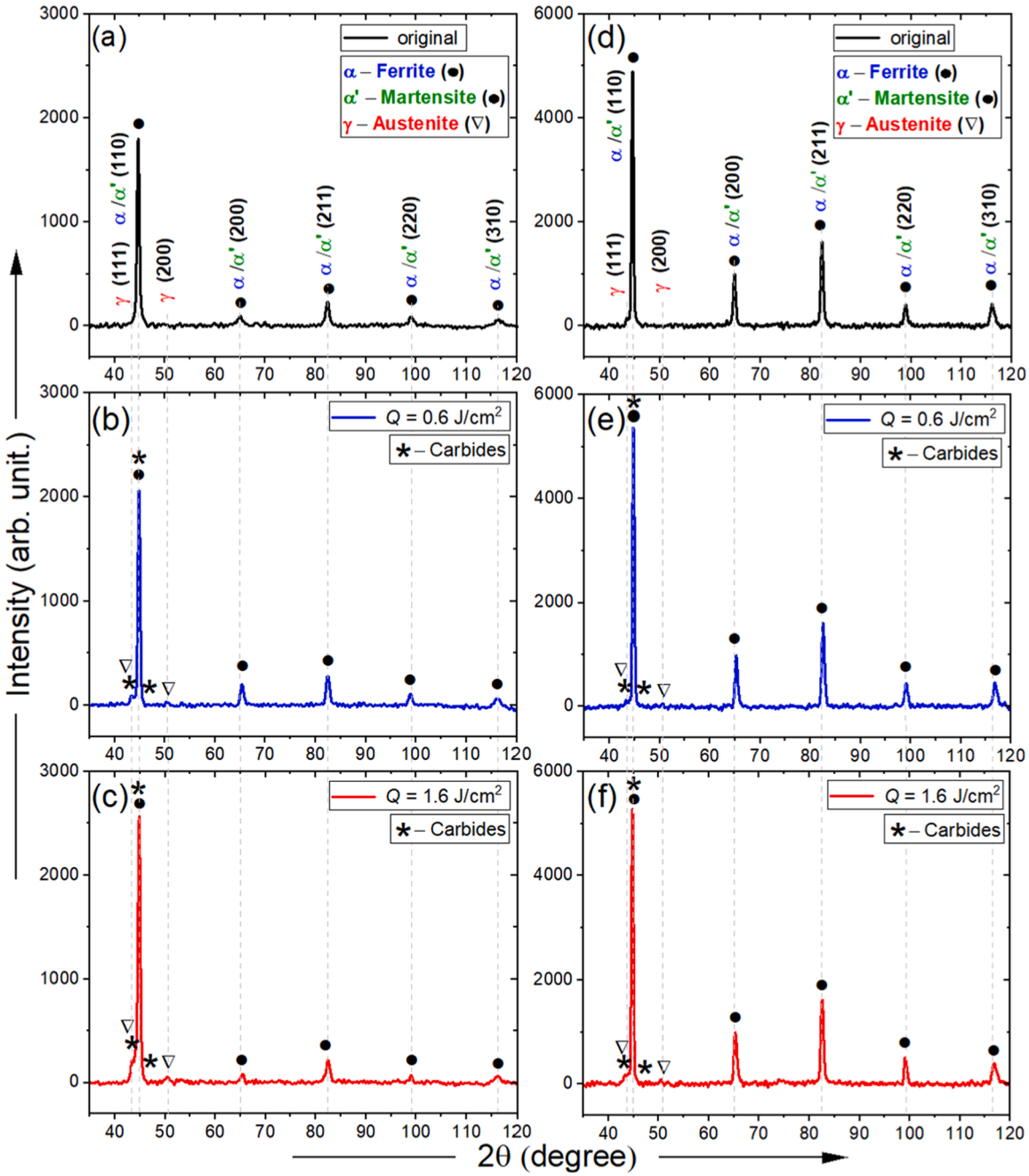

Fig. 7. X-ray patterns of steel specimens before (a, d) and after IPIB treatment (b, c, e, f) with different current densities obtained in GIXRD (a-c) and Bregg-Brentano (d-f) geometries.

melting of the surface layer of the target, its cooling at very high speeds (~10^9 K/s), excitation of stress waves (deformations), mixing the components of the molten layer. The observed change in the uniformity of the chemical composition is caused by convective and advective mixing of the melt.

The high concentration of vacancies formed during high-speed cooling accelerates the diffusion of carbon and manganese impurity atoms, which leads to their enrichment of the near-surface layer and the formation of new phases (Fig. 10), in addition, the processes of mixing (and displacement of impurities) in the molten layer can also contribute. High cooling rates during crystallization can cause structural and phase transformations with the formation of a supersaturated solid solution and its decomposition with the release of metastable phases [3].

In steels, as shown in [37], carbide transformations can occur without changing the size and shape of particles in the following sequence: $Fe_7C_3 \rightarrow Fe_5C_2 \rightarrow Fe_3C$, therefore, their formation during surface treatment of IPIB is quite natural. However, it should be noted that the presence of manganese, hydrogen, oxygen and the imbalance of the process can change this sequence.

The combined effect of high temperature and stresses arising in the target under the action of IPIB is complex [3] and can affect changes in the characteristics of the fine structure. Minor changes in the phase lattice parameter, the insignificant increases in the size of the coherent scattering regions L and the decrease in the magnitude of microstrain $\frac{\Delta d}{d}$ (Table 1) may be the result of repeated quenching during cooling of the molten surface layer. Similar changes in the structure and phase composition in steels treated with pulsed beams of charged particles were observed in [8–10]. For example, the authors of [10] did not detect changes in composition in the sample using EDX, however, studies

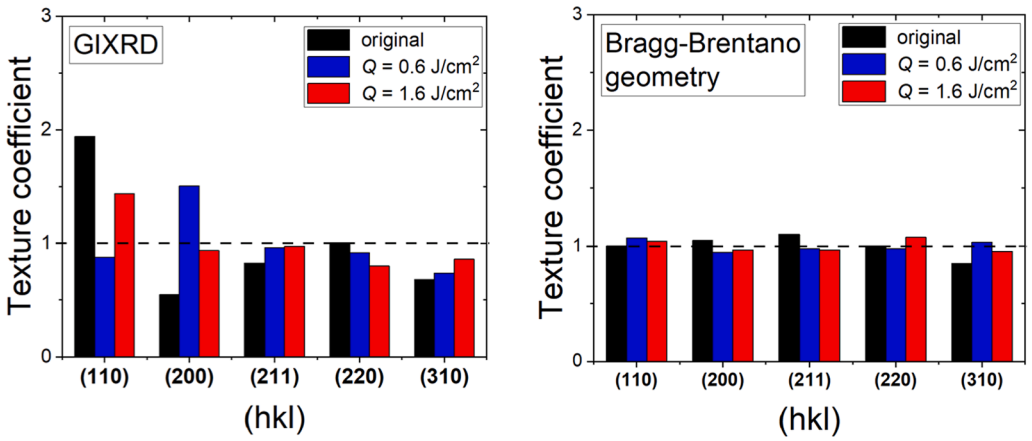

Fig. 8. Texture coefficients of samples before and after IPIB exposure obtained in GIXRD and Bregg-Brentano geometries.

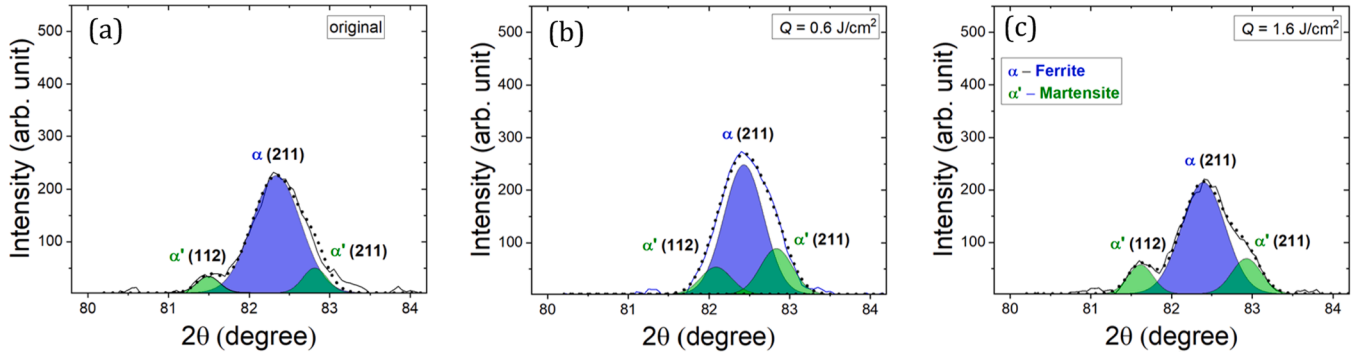

Fig. 9. Fragments of X-ray patterns (GIXRD) in the diffraction angles interval 2θ = 78.8-84.2 degree of the samples treated with different current densities.

Table 1
Structural characteristics of the phases of steel treated with IPIB: lattice parameters a and c, size of the coherent scattering regions L, magnitude of microstrain $\frac{\Delta d}{d}$, concentration carbon in martensite C.

Phase, space group	Structure parameters	Processing modes		
		original	$Q = 0.6$ J/cm^2	$Q = 1.6$ J/cm^2
Ferrite *Im3m* (229)	a (nm)	0.2866	0.2864	0.2865
	L (nm)	19	21	22
	$\frac{\Delta d}{d}\times10^3$	3.3	2.9	2.7
Martensite *I4/mmm* (139)	a (nm)	0.2840	0.2845	0.2837
	c (nm)	0.2917	0.2888	0.2913
	c/a	1.027	1.015	1.027
	C (wt. %)	0.65	0.25	0.65

conducted using transmission electron microscopy revealed nanoscale carbide particles in the near-surface layer, the appearance of which the authors associate with crystallization, accompanied by the release of phases other than those that existed before irradiation.

Mechanical and elastoplastic characteristics calculated from the results of indentation (hardness H, elastic modulus E, elastic reverse deformation work of indentation W_{el}, total mechanical work of indentation W_{total}, indentation relaxation R) and friction coefficient μ of the specimens are presented in Table 2. IPIB treatment leads to a decrease in hardness H of the steel surface layer by 44 and 56 % for $Q = 0.6$ and 1.6 J/cm^2, respectively. The character of elastic modul's E, determined by the Oliver-Farr method [38], changes under different conditions of IPIB irradiation is similar to that of hardness H. The observed effect of decreasing hardness and elastic modulus (Fig. 11a, d, g, Table 2) of the samples with depth is associated with thermal effects, stresses in the near-surface layer under conditions of rapid heating and cooling, martensite decomposition and growth of the volume fraction of the ferrite phase [28]. Noticeable changes in elastoplastic characteristics – elastic modulus E, elastic strain work W_{el}, total work done during indentation W_{total}, elastic recovery R – can also be seen. The total work of deformation $W_{total} = W_{el} + W_{pl}$ done during indentation is spent mainly on plastic deformation W_{pl}, while IPIB exposure leads to an increase in elastic work W_{el} and indentation relaxation R. IPIB treatment leads to an increase in the elastic recovery $R = \frac{h_{max}-h_0}{h_{max}}$ of the specimens in the indentation region (Table 2), thereby giving the near-surface layer an elastic state.

Fig. 12 shows micrographs of oblique sections with a plane made at an angle 3 degree, texture and reverse pole figures of phases (martensite and ferrite) included in the samples before and after treatment with $Q = 1.6$ J/cm^2. It can be seen that under the influence of treatment there is a change in grain size, and at depths from $h_1 \approx 0.3$ μm to $h_2 \approx 0.5$ μm (Fig. 12), corresponding to the maximum of radiation damage, a layer consisting mainly of ferrite is formed. The hardness and modulus of elasticity of samples after IPIB treatment decreases compared to the initial value due to the decomposition of harder martensite and the formation of a layer consisting mainly of softer ferrite, as noted in [28].

To quantify the resistance of modified layers to mechanical contact effects, the H/E and H^3/E^2 ratios are used, showing their resistance to wear and plastic deformation [39], respectively. As shown in Table 2, the value of H/E does not change noticeably, while H^3/E^2 decreases monotonically. The observed decrease in the friction coefficient after IPIB is caused by the modification of the near-surface layer of the samples as a result of changes in its structural-phase state. The abrasive particles (wear products) formed in the process of friction have different hardness, shape and size. Analysis of SEM-BSD images of wear tracks

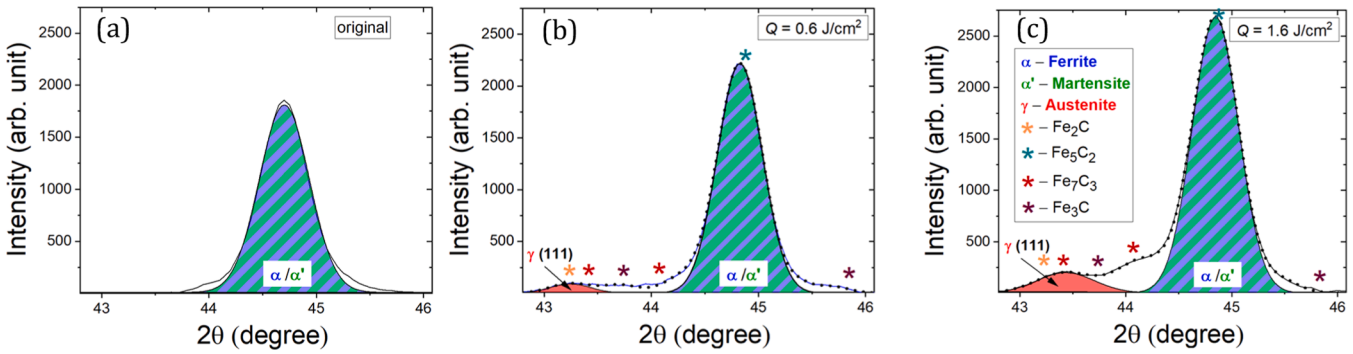

Fig. 10. Fragments of X-ray patterns (GIXRD) in the diffraction angles interval 2θ = 42.8-46.2 degree of the samples treated with different current densities.

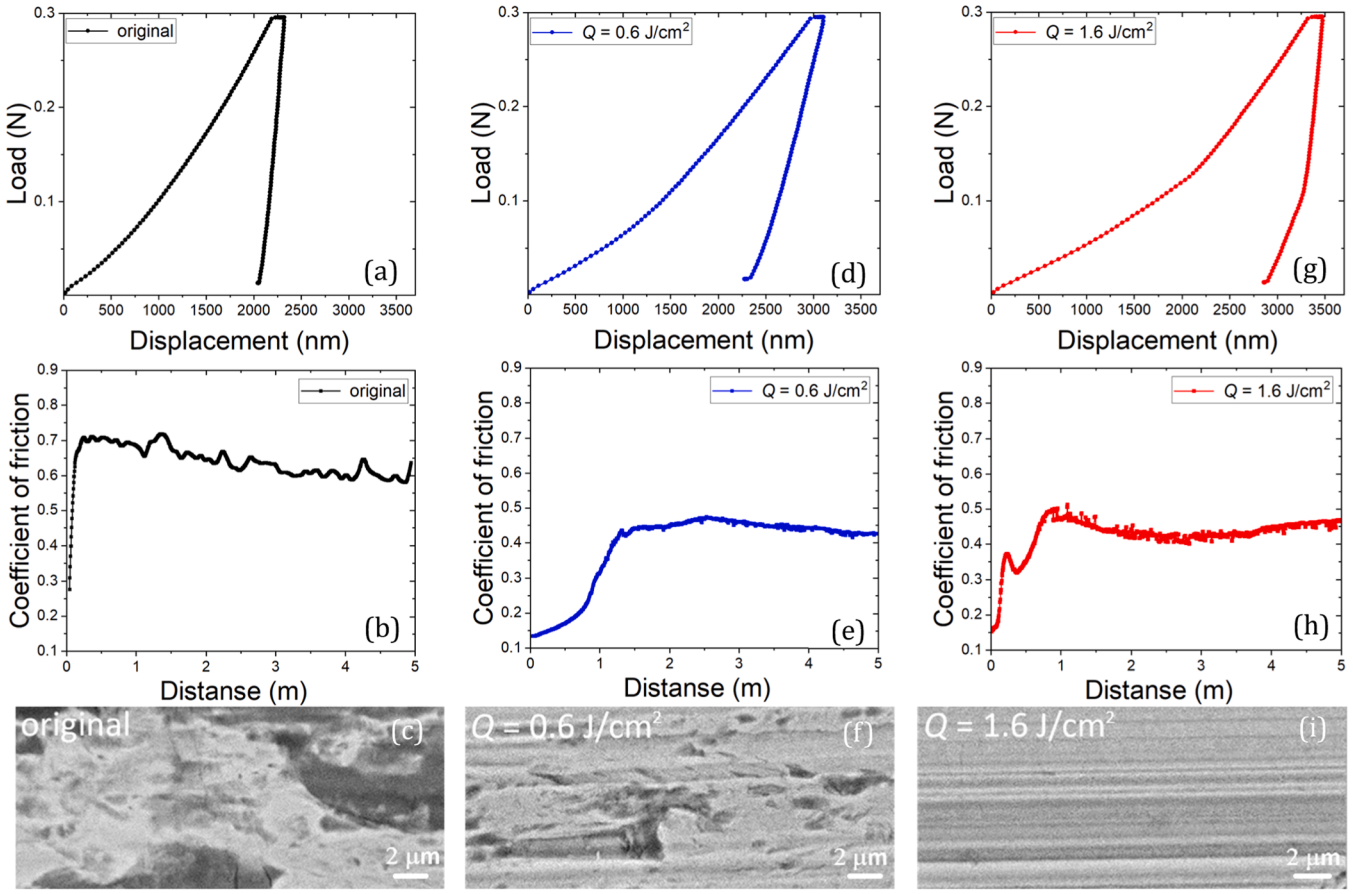

Fig. 11. Load-displacement curves, coefficient of friction and SEM-BSD images wear tracks of IPIB-treated samples.

Table 2
Elastoplastic and tribomechanical properties of samples of carbon steel 65 treated with an IPIB.

Treatmend	H (GPa)	E (GPa)	H/E	H^3/E^2 (GPa)	W_{el} (mN×μm)	W_{total} (mN×μm)	R (%)	μ
original	2.5±0.23	202±18	0.012	0.00038	36	313	12	0.62
$Q = 0.6$ J/cm^2	1.4±0.13	101±9	0.014	0.00027	109	406	27	0.42
$Q = 1.6$ J/cm^2	1.1±0.10	117±11	0.010	0.00010	61	422	18	0.45

demonstrates different wear mechanism (Fig. 11c, f, i): for the original specimen an adhesive mechanism is observed, for the treated one with $Q = 1.6$ J/cm^2 – an abrasive one, and with $Q = 0.6$ J/cm^2 – a mixed one. The prevailing physical phenomenon that affects the change in the characteristics of the near-surface layer at irradiation with Q < 1 J/cm^2 is the radiation-dynamic effect of IPIB (formation of defects, shock waves), and at Q ≥ 1 J/cm^2 - the thermal effect (melting and recrystallization).

4. Conclusion

Studies have shown that treating the surface of steel 65 with a hydrogen (30%) and carbon (70%) at accelerating voltage of 250 kV and an energy density of 0,6 and 1,6 J/cm^2 with a single pulse duration of

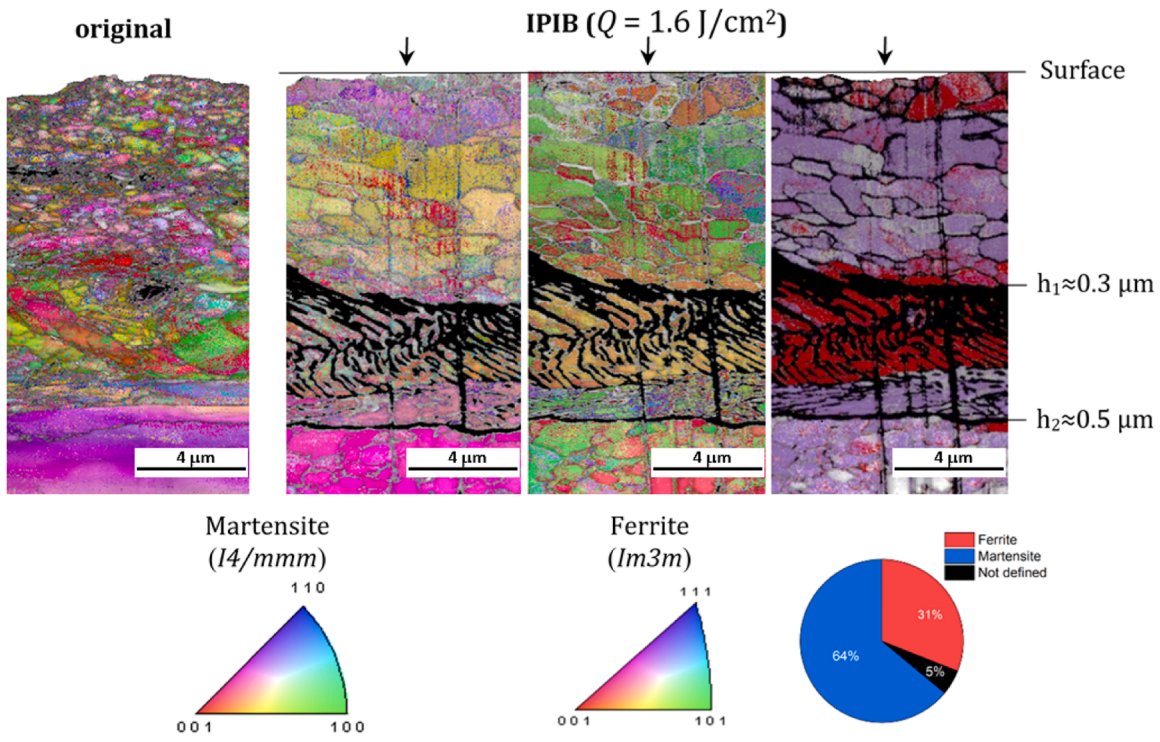

Fig. 12. FIB-cross-sectional images (oblique grinding in 3 degree) and SEM-EBSD microstructure of samples after the IPIB irradiation with Q = 1.6 J/cm^2. Insets show standard stereographic triangles and color matching.

100 ns leads to a change in the state of its surface: smoothing of the relief (the average roughness of *Ra* decreases 2-3 times compared to the initial value), the formation of craters, an increase in their average diameter from 4 to 6 μm and surface density from $2{\cdot}10^8$ to $8{\cdot}10^8$ m^{-2} with increasing energy density; a change in the predominant orientation of crystallites in the near-surface layer, comparable in magnitude to the projective range of ions; formation of new phases and an increase in their volume fraction with an increase in energy density. There is a decrease in hardness, elastic modulus and a change in the wear character of the near-surface layer. The coefficient of friction decreases by a factor of 1.5.

Declaration of competing interest

The authors declare that they have no known competing financial interests or personal relationships that could have appeared to influence the work reported in this paper.

CRediT authorship contribution statement

Natallia Poliak: Writing – review & editing, Writing – original draft, Visualization, Methodology, Investigation, Formal analysis, Data curation, Conceptualization. **Victor Anishchik:** Writing – review & editing, Resources, Methodology, Conceptualization.

Declaration of competing interest

"There are no competing interests to declare".

Acknowledgements

The authors thank Dr. V.A. Tarbokov (Tomsk Polytechnic University) for sample irradiation assistance.

Data availability

No data was used for the research described in the article.

References

[1] T.J. Renk, P.P. Provencio, S.V. Prasad, A.S. Shlapakovski, A.V. Petrov, K. Yatsui, W. Jiang, H. Suematsu, Materials modification using intense ion beams, in: Proc. IEEE92, 2004, pp. 1057–1081, https://doi.org/10.1109/JPROC.2004.829024.
[2] G.E. Remnev, V.A. Tarbokov, S.K. Pavlov, Material modification by high-intense pulsed ion beams, Inorg. Mater. Appl. Res. 13 (2022) 626–640, https://doi.org/10.1134/S2075113322030327.
[3] A.D. Pogrebnjak, O.P. Kul'ment'eva, Structural-phase transformations in near-surface layers and properties of metal materials after pulse influence to particle beams, Phys. Surf. Eng. 1 (2003) 108–206.
[4] A.Ya. Leyvi, K.A. Talala, V.S. Krasnikov, A.P. Yalovets, Modification of the constructional materials with the intensive charged particle beams and plasma flows, Bull. South Ural State Univ. Ser. Mech. Eng. Indus. 16 (2016) 28–55, https://doi.org/10.14529/engin160103.
[5] A.D. Pogrebnjak, V.S. Ladysev, N.A. Pogrebnjak, A.D. Michaliov, V.T. Shablya, A. N. Valyaev, A.A. Valyaev, V.B. Loboda, A comparison of radiation damage and mechanical and tribological properties of α-Fe exposed to intense pulsed electron and ion beams, Vacuum 58 (2000) 45–52, https://doi.org/10.1016/S0042-207X(00)00221-9.
[6] G.E. Remnev, V.A. Shulov, Application of high-power ion beams for technology, Laser Part. Beams. 11 (1993) 707–731, https://doi.org/10.1017/S0263034600006467.
[7] L.L. Meisner, A.B. Markov, D.I. Proskurovsky, V.P. Rotshtein, G.E. Ozur, S. N. Meisner, E.V. Yakovlev, T.M. Poletika, S.L. Girsova, V.O. Semin, Effect of inclusions on cratering behavior in TiNi shape memory alloys irradiated with a low-energy, high-current electron beam, Surf. Coat. Technol. 302 (2016) 495–506, https://doi.org/10.1016/j.surfcoat.2016.06.036.
[8] N.I. Poliak, V.M. Anishchik, Microstructure and physico-mechanical properties of steel, processed by a pulsed electron beam, Phys. Chem. Mater. Treat. 4 (2024) 5–15, https://doi.org/10.30791/0015-3214-2024-4-5-15.
[9] N.I. Poliak, V.M. Anishchik, V.V. Khodasevich, Changes in the near-surface layer of steel processed by a pulsed electron beam, J. Belarus. State Univ. Ser. Phys. 2 (2024) 84–92. https://journals.bsu.by/index.php/physics/article/view/6205.
[10] H. Wang, L. Li, S. Qiu, Zhai, W.Q. Li, W. Zhai, Q. Li, S. Hao, Evolution of microstructure at the surface of 40CrNiMo7 steel treated by high-current pulsed electron beam, Coatings 10 (2020) 311–321, https://doi.org/10.3390/coatings10040311.
[11] H.K.D.H. Bhadeshia, R.W.K. Honeycombe, Steels. Structure, properties and design, fifth ed., 2024. https://doi.org/10.1016/C2022-0-00193-8.

[12] E.J. Mittemeijer, M.A.J. Somers, Thermochemical surface engineering of steels: improving materials performance, 2015. https://doi.org/10.1016/C2013-0-16318-0.
[13] X. Yu, J. Shen, M. Qu, H. Zhong, J. Zhang, Y. Zhang, Sh. Yan, G. Zhang, X. Zhang, X. Le, Distribution and evolution of thermal field formed by intense pulsed ion beam on thin metal target, Nucl. Instrum. Methods B. 365 (2015) 225–229, https://doi.org/10.1016/j.nimb.2015.07.061.
[14] Z.H. Dong, C. Liu, X.G. Han, M.K. Lei, Induced stress wave on the materials surface irradiated by high-intensity pulsed ion beam, Surf. Coat. Technol. 201 (2007) 5054–5058, https://doi.org/10.1016/j.surfcoat.2006.07.149.
[15] A.I. Pushkarev, Yu.I. Egorova, S.S. Polisadov, Effect of long-range interaction in the modification of near-surface layers of WC–Co samples by pulsed ion beam, J. Surf. Investig. 18 (2024) 222–228, https://doi.org/10.1134/S1027451024010348.
[16] A.D. Korotaev, A.N. Tyumentsev, Yu.P. Pinzhin, G.E. Remnev, Features of the morphology, defect substructure, and phase composition of metal and alloy surfaces upon high-power ion beam irradiation, Surf. Coat. Technol. 185 (2004) 38–49, https://doi.org/10.1016/j.surfcoat.2003.11.021.
[17] G.V. Potemkin, O.K. Lepakova, V.D. Kitler, M.V. Zhidkov, M.S. Syrtanov, A.E. Ligachev, Phase transformations in nitrided ferrovanadium under the action of a high power carbon ion beams, Inorg. Mater. Appl. Res. 12 (2021) 615–624, https://doi.org/10.1134/S207511332103031X.
[18] H. Akamatsu, T. Ikeda, K. Azuma, E. Fujiwara, M. Yatsuzuka, Surface treatment of steel by short pulsed injection of high-power ion beam, Surf. Coat. Technol. 136 (2001) 269–272, https://doi.org/10.1016/s0257-8972(00)01029-x.
[19] M.V. Zhidkov, A.E. Ligachev, E.V. Golosov, M.Y. Gazizova, S.K. Pavlov, G. E. Remnev, Study of craters formed on surface of AISI 321 stainless steel after high power ion-beam exposure, Vacuum 198 (2022) 110852, https://doi.org/10.1016/j.vacuum.2021.110852.
[20] V.S. Krasnikov, A.Ya. Leyvi, A.E. Mayer, A.P. Yalovets, Surface microrelief smoothing mechanisms in a target irradiated by an intense charged particle beam, Tech. Phys. 52 (2007) 431–439, https://doi.org/10.1134/s1063784207040068.
[21] X. Wang, M.K. Lei, J.S. Zhang, Surface modification of 316L stainless steel with high-intensity pulsed ion beams, Surf. Coats. Technol. 201 (2007) 5884–5890, https://doi.org/10.1016/j.surfcoat.2006.10.040.
[22] V.A. Shulov, A.S. Novikov, A.G. Paikin, A.B. Belov, A.F. Lvov, G.E. Remnev, Crater for mation on the surface of refractory alloys during high-power ion-beam processing, Surf. Coat. Technol. 201 (2007) 8654–8658, https://doi.org/10.1016/j.surfcoat.2006.01.078.
[23] H. Zhong, J. Zhang, J. Shen, G. Liang, S. Zhang, M. Xu, M. Xu, X. Yu, S. Yan, G. E. Remnev, X. Le, Dynamic mechanism of crater formation induced by inclusion during intense pulsed ion beam irradiation, Vacuum 179 (2020) 109541, https://doi.org/10.1016/j.vacuum.2020.109541.
[24] N.B. Volkov, A.E. Mayer, A.P. Yalovets, On the mechanism of cratering on solid surfaces exposed to an intense charged particle beam, Tech. Phys. 47 (2002) 968–977, https://doi.org/10.1134/1.1501675.
[25] V.I. Boiko, A.N. Valyaev, A.D. Pogrebnyak, Metal modification by high-power pulsed particle beams, Phys. Usp. 42 (1999) 1139–1166, https://doi.org/10.1070/PU1999v042n11ABEH000471.
[26] B. Han, S. Yan, X. Le, W. Zhao, G. Remnev, M. Opekounov, I.F. Isakov, I. Grushin, The phase and microstructure changes in 45# steel irradiated by intense pulsed ion beams, Surf. Coat. Technol. 128-129 (2000) 387–393, https://doi.org/10.1016/s0257-8972(00)00641-1.
[27] V.K. Struts, G.E. Remnev, Investigation of the impact of pulsed high-power ion beams on P6M5 tool steel, Izvestiya Vuz. Fizika. (2010) 125–128.
[28] T.V. Panova, V.S. Kovivchak, D.V. Zhukov, V.I. Blinov, Rentgenographic study changes in the near-surface layers of turbine blades under irradiation high-powered ion beam, Bull. Omsk Univ. 2 (2005) 21–23.
[29] X. Li, R. Wang, Q. Wang, J. Guo, R. Xian, Scanning electron beam polishing and defect analysis of 65 steel, Nuclear Inst. Method. Phys. Res., B. 490 (2021) 34–38, https://doi.org/10.1016/j.nimb.2020.11.015.
[30] ISO 14577-1:2015. Metallic materials – Instrumented indentation test for hardness and materials parameters – Part 1: Test method, 2015.
[31] G. Nolze, A. Winkelmann, G. Cios, T. Tokarski, Tetragonality mapping of martensite in a high-carbon steel by EBSD, Materials Characterization 175 (2021) 111040, https://doi.org/10.1016/j.matchar.2021.111040.
[32] J.F. Ziegler, M.D. Ziegler, J.P. Biersack, SRIM – The stopping and range of ions in matter, Nucl. Instrum. Methods B. 268 (2010) 1818–1823, https://doi.org/10.1016/j.nimb.2010.02.091.
[33] G.B. Harris, Quantitative measurement of preferred orientation in rolled uranium bars, Phil. Mag. 43 (1952) 113–123, https://doi.org/10.1080/14786440108520972.
[34] R. Roberti, Preferred orientation in drawn austenitic stainless steel, Metall. Res. Technol. 5 (1987) 21–25.
[35] T.V. Panova, V.I. Blinov, V.S. Kovivchak, G.I. Gering, D.V. Konstantinov, Formation of preferred orientations in aluminum, copper and nickel irradiated with intense ion beams, J. Surf. Invest.: X-Ray, Synchrotron Neutron Tech. 1 (2007) 197–203, https://doi.org/10.1134/s1027451007020164.
[36] G.E. Remnev, Modification of materials using powerful ion beams, Bull. Tomsk. Polytechnic Univ. 303 (2000) 59–70.
[37] V.M. Shchastlivtsev, N.I. Medvedeva, V.S. Kraposhin [and others], Cementite in carbon steels, Ed. by V.M. Shchastlivtsev, Educational and Methodological Center of the Ural Polytechnic Univ. Publ., 2017.
[38] W.C. Oliver, G.M. Pharr, An improved technique for determining hardness and elastic modulus using load and displacement sensing indentation experiments, J. Mater. Res. 7 (1992) 1564–1583, https://doi.org/10.1557/JMR.1992.1564.
[39] A. Leyland, A. Matthews, On the significance of the H/E ratio in wear control: a nanocomposite coating approach to optimised tribological behavior, Wear 246 (2000) 1–11, https://doi.org/10.1016/S0043-1648(00)00488-9.